RICE UNIVERSITY

# Design, Construction, and Commissioning of the Time-of-Flight Detector for BNL-AGS Experiment 896

by

## Christopher L. Stokely

A THESIS SUBMITTED
IN PARTIAL FULFILLMENT OF THE
REQUIREMENTS FOR THE DEGREE

## Master of Arts

APPROVED, THESIS COMMITTEE:

William J. Llope, Faculty Fellow, Director
Department of Physics

Marjorie D. Corcoran, Professor
Department of Physics

Huey W. Huang, Professor
Department of Physics

Houston, Texas

February, 1998

# Abstract

# Design, Construction, and Commissioning of the Time-of-Flight Detector for BNL-AGS Experiment 896

by

Christopher L. Stokely

A Time-of-Flight (TOF) detector is used to provide particle identification in BNL-AGS Experiment 896. It is also used to assist in tracking and as a fast trigger. Results are presented from simulations which optimized the dimensions and position of the TOF system. Rates for measuring daughters of certain strange neutral particles are given for several cuts. Based on these simulation results, TOF detectors were added to the experiment. The analysis of data from a 1997 heavy ion beam run and a 1997 secondary beam run are discussed. From this data, evidence for significant correlated noise is observed. The best method to estimate the location of the minimum ionizing peak of the ADC distribution was found among several different methods. Two different methods to slew correct the TDC data are investigated. Effects of momentum variance and path length variance on the time resolution of one of the TOF detector slats are studied. Plans to improve the detector for the upcoming 1998 heavy ion beam run are also discussed.

# Acknowledgements

Finishing this Thesis, I would like to thank the following people both inside and outside the E896 Collaboration:

●my thesis advisor, William J. Llope, who showed faith in me by giving such an important role in the TOF detector. In addition to physics, he taught me much about the art of programming;

● to the E896 spokespersons Hank Crawford (UC-SSL) and Tim Hallman (BNL), for their constant encouragement during my stay at BNL;

● to King Chan, for him building the Rice TOF walls with Dr. Llope;

● to John W. Mitchell and Gerard Visser for going far beyond the call of duty to help get the TOF detector data;

● to Kris Kainz, the other graduate student in our group, for his tireless help, intelligent comments, sense of humor, and for our good friendship;

● to Elisabeth Mogavero, for all her assistance, especially during the winter of 1997;

● to my good friend Salvo Costa (INFN-Catania), for his uncalled for help in getting the TOF detector working;

● and to my other collaborators in E896 for their their intellectual comments, technical support, and their friendship.

# Contents

# I.  Introduction to BNL Experiment 896

Experiment 896 is a fixed target experiment at the Brookhaven National Laboratory (BNL) Alternating Gradient Synchrotron (AGS). It uses an $\sim$11.7 GeV/c per nucleon $^{197}$Au beam on a fixed $^{197}$Au target. E896 was designed to search for the $H_0$ dibaryon, a short-lived neutral particle with a six quark *uuddss* content.[1]  The existence or nonexistence of the $H_0$ dibaryon places strong contraints on various models which either predict or refute the $H_0$. [2] In addition to the $H_0$ search, E896 was designed to study the production of $\Lambda$ and $\overline{\Lambda}$ hyperons and $K_s^0$ mesons in relativistic $^{197}$Au + $^{197}$Au collisions. Experiment 896 is efficient in measuring the following weak decay channels: $H_0 \rightarrow p + \Sigma^- \rightarrow p + n + \pi^-$, $\Lambda \rightarrow p + \pi^-$, $\overline{\Lambda} \rightarrow \overline{p} + \pi^+$, and $K_s^0 \rightarrow \pi^+ + \pi^-$.

In the original Proposal 896 [3], only tracking information was to be used in the search for the $H_0$. There are, however, several backgrounds that can resemble $H_0$ decay topologies, which are secondaries produced from neutron and gamma interactions with the materials of the Distributed Drift Chamber (DDC), the major tracking detector of E896. There are similar backgrounds for the reconstruction of the $\Lambda$, $\overline{\Lambda}$, and $K_s^0$. Combining direct particle identification with DDC tracking dramatically reduces these backgrounds. [4]

A time-of-flight (TOF) detector can provide the velocities of particles for which the momentum and full path length are known from DDC tracking. Below specific

---

[1]It was first predicted by Jaffe using the MIT bag model. [1]

momenta, the velocities "group" according to the very different masses of pions, kaons, and protons. This allows one to place cuts on plots of track velocity versus momentum to directly identify the species for each track.

In addition to providing Particle Identification (PID), a TOF detector can assist in the reconstruction of DDC tracks by providing positions of particle hits on the TOF detector after a long flight path. A TOF detector can also be used as a fast trigger for daughters of rare particles.

For these three reasons, a TOF detector was designed for E896 using GEANT simulations. These simulations determined the optimal TOF detector configuration among several possible options and under a number of contraints. This TOF detector design will be shown to provide reasonable efficiencies for identifying the daughters of $H_0$ dibaryons, $\Lambda$ and $\overline{\Lambda}$ hyperons, and $K_s^0$ mesons.

The detector so designed was then constructed. The TOF detector and its hardware and electronics will be discussed in Section IV. Analysis results from the January 1997 $^{197}$Au run and the May 1997 charge one secondary beam run at the AGS will be presented in section V. The summary and the discussion of the future plans are given in section VI.

## II.    Experimental overview of E896

Figure 1 shows a top view of the E896 setup as originally proposed. Also shown is the path of the noninteracting gold beam. Starting on the left side of Figure 1,
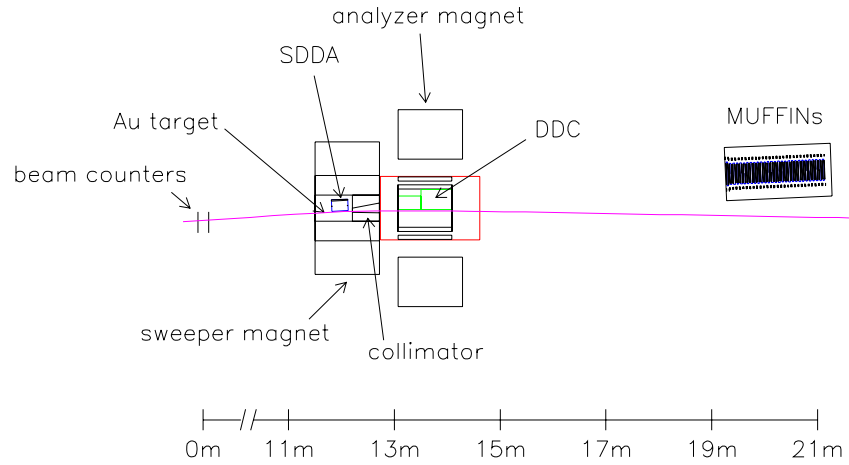
**Figure 1:** Top view of E896.

the beam first passes through two beam counters, which provide the start time for each event. Each beam counter consists of a $200\mu$m thick quartz Cerenkov radiator viewed by two very fast Hamamatsu 2038 PhotoMultiplier Tubes (PMTs). These beam counters were shown in BNL-AGS E877 to have a time resolution on the order of 25ps. [5]

About 12m downstream of the beam counters, the beam passes through a thin gold target located in the sweeper magnet. Next to the target is the Silicon Drift Detector Array (SDDA), which is a tracking detector for particles that decay close to the target.

Downstream of the SDDA is a tungsten collimator. The strong 4.7T vertical field of the sweeper magnet deflects many of the charged particles from beam-target collisions into the collimator so that the charged particles from these collisions do

not "swamp" the charged decay products of the $H_0$, $\Lambda$, $\overline{\Lambda}$, and $K_s^0$. This provides for a relatively clean environment for neutral particle decay searches in the detectors downstream of the collimator.

Downstream of the sweeper magnet is the analyzer magnet and the Distributed Drift Chamber (DDC) is positioned in its bore. The DDC consists of 144 wire chamber planes. The paths of charged particles that traverse the DDC are curved by the 1.7T vertical field of the analyzer magnet, allowing the momentum and positions of DDC tracks to be determined.

About 6m downstream of the DDC is the Multi-Functional Neutron Spectrometer (MUFFINs). It will be used in identifying neutrons from various predicted decays of the $H_0$ dibaryon.

With this original detector layout of E896, a TOF detector was designed using GEANT simulations. The TOF system will rely on the DDC to provide momenta and path lengths of DDC tracks that hit the TOF walls. The TOF detector will also rely on the beam counters to provide the start times for each event. The simulations are described in the following section.

## III. Optimization of the Design

### A. Introduction to Geant Simulations

Simulations were done to optimize the arrangement of the TOF system prior to its construction, and to simulate the performance of the TOF system for the development

of analysis software. GEANT was developed at CERN and is commonly used in high energy nuclear physics to design detectors. It is a library of Fortran routines that simulate particle trajectories, their deflections in a magnetic field, their energy losses in materials, their decays, and so on.

Files are read in by GEANT to specify the size, position, and material composition of all volumes within the software version of the experiment. The magnetic fields used in these simulations were Tosca model generated field maps. [6] An event is started by specifying the momentum, initial position vertex, and species of each particle. Full kinematics of particles that hit the TOF detector are stored in N-tuple format.[2] In addition, full kinematics of the parents of the particles that hit the TOF detector are also stored.

These simulations investigate the sensitivity of various TOF geometries to the daughters of $H_0$ dibaryons, $\Lambda$ and $\overline{\Lambda}$ hyperons, and $K^0_s$ mesons. The TOF detectors must be sensitive to low momentum pions from $H_0$, $\Lambda$, and $\overline{\Lambda}$ decays, high momentum pions from $K^0_s$ decays, high momentum protons from $H_0$ and $\Lambda$ decays, and high momentum antiprotons from $\overline{\Lambda}$ decays. The TOF detector width is determined by the lowest momentum positive and negative daughters of these four different parent types, which are the negative pions from $\Lambda$ decays and the positive pions from $\overline{\Lambda}$ decays.

---

[2] The exact values of the data are stored in a table-like format called an N-tuple.

The simulations will investigate the multiple hit probabilities of the TOF slats. The position of the TOF detector and the width of its slats determine these probabilities. The goal was to minimize these probabilities by varying TOF detector positions and slat widths. One wants to minimize these probabilites since TOF data is much more difficult to analyze when more than one charged particle hits a single slat in an event.

A number of different geometrical configurations of the TOF system were studied. Included in these different configurations is an existing detector built by McGill University for the previous BNL-AGS Experiment 877. The Rice University group assumed control of this TOF detector.

The specific restrictions on the possible geometries are as follows:

• The MUFFINs detector placement was fixed and the TOF detectors have to be placed either in front and/or behind the MUFFINs.

• At least 2 meters had to be left free downstream of the analyzer for DDC mounting and access.

• Due to cost considerations, approximately 45 TOF slats were the maximum number of slats that could be built to augment the existing wall.

• There were space constraints from radiation shielding blocks because of an experiment adjacent to the E896 beam area.

The goal was to design the optimal TOF system under these constraints that is a combination of the E877 wall plus one to two additional walls which would be built at Rice University. The event types and cuts used in these simultions are now described.

## B. Event Generation within the E896 UT Geant

There were three methods to generate the events for input to GEANT: HIJET events, Monte Carlo events, and Fiducial events.

- **Hijet events:** These are complete events of 11.6 GeV/c per nucleon $^{197}$Au on a fixed $^{197}$Au target generated using the HIJET model. [7] These events are stored in a text file which contains the particle ID and three-vector momentum for all of these particles in each event. GEANT reads this file and propagates these particles starting from the target.

Processing complete events is extremely CPU intensive and time consuming. For much quicker but also accurate studies of the efficiencies for measuring decay daughters in the TOF system, so-called Monte Carlo events and Fiducial events are used.

- **Monte Carlo (MC) events:** These events include only one particular parent type, *i.e.* $\Lambda$, $\overline{\Lambda}$, or $K_s^0$, emitted from the target. The multiplicity per event of these parents is sampled from probability distributions obtained from the complete HIJET events. For each particle, the rapidity and transverse momenta are sampled from the two-dimensional (y,$P_t$) distributions obtained from the complete HIJET events.

- **Fiducial (Fid) events:** These include only one parent per event, either a $\Lambda$, $\overline{\Lambda}$, $K_s^0$, or $H_0$, that decays within the fiducial volume of the DDC. These events are

stored in a text file, which contains both the position of the decay vertex and the three-vector momenta of the particular parent particle. The single particle fiducial events are read into GEANT, and the lifetime of the parent under study is made arbitrarily small so that it decays immediately.

To generate the fiducial event file, a rapidity and transverse momentum for each parent particle is sampled from distributions obtained from the complete HIJET events. In addition, each parent particle is assigned a sampled lifetime, dilated in the lab frame. The momentum and the lifetime of the parent particle are used to determine if it decays within the bounds of the DDC. If so, the three-vector momentum and three-vector decay vertex are saved. The overall probability for these fiducial decays is also saved to allow the scaling of the numbers of these events to the equivalent number of complete events.

These events are studied since the presence of the decay vertex in the fiducial volume of the DDC provides the cleanest possible measurement of the parent decay. However, the rates for these decays are much lower than MC events, which include decays upstream of the DDC.

In the Fid events, the $H_0$ is assumed to have a lifetime of $c\tau \approx 4\text{cm}$, mean rapidity $\mu_y = 1.57$, gaussian rapidity distribution width $\sigma_y = 0.5$, and transverse momentum $P_t$ = 200MeV/c. In both the Fid events and the MC events, the rapidity and transverse momentum distributions of the $\overline{\Lambda}$ were assumed to be the same as the $\Lambda$. [3]

---

[3]This was done since there is currently very little spectral data for the $\overline{\Lambda}$.

## C.  Cuts on the Simulated Data

The simulation results for a certain progression of cuts on the simulated data will be discussed below. These cuts are intended to be similar to those imposed by the experiment and the analyses.

**CUT 1** : To pass this cut, a particle must hit a TOF slat. This cut therefore imposes the geometrical efficiency of the TOF system for detecting a particular particle, daughter or otherwise.

**CUT 2** : This cut requires that a track associated with a hit in the TOF wall pass through at least 10cm of the fiducial volume of the DDC. For daughters that pass this cut, it is assumed that the momentum and path length of the particle can be obtained from the DDC (each with a resolution that can be adjusted within the simulations). This cut is a minimal requirement on the "trackability" of the particles that passed Cut 1, as the TOF relies on the DDC for determining the momentum and path lengths of tracks.

**CUT 3** : This cut requires that both daughters of a particular parent pass Cuts 1 and 2. It is at this level where the simulation results are specific to the measurement of a particular parent particle.

**CUT 4** : This cut requires that the daughter momenta is less than the maximum momenta for which the daughter can be positively identified on the basis of its TOF. These cut-off momenta were determined using complete events and estimates for the DDC momentum resolution ($\Delta p/p$ in the range 1-2%) and TOF resolution (80-120 ps). These resolutions are expected to be similar to those in the actual experiment. Tracks that pass this cut are directly identified.

## D.   Comparison of Different TOF Geometries

The performance of three different configurations, called options A, B, and C, were compared. For each option, the multiple hit probabilites, geometrical efficiencies, and the efficiencies for direct PID were studied. Top views of the experiment for the the various options are shown in Figure 2. In option A, a wide downstream wall is positioned in front of the MUFFINs detector. In options B and C, two downstream walls are positioned on beam left and beam right of the MUFFINs.[4]

The upstream wall is used to measure the low momentum pions from the decays of the $\Lambda$, $\overline{\Lambda}$, and $H_0$. The downstream wall is used to measure the high momentum pions from $K_s^0$ decays, high momentum protons from $\Lambda$ and $H_0$ decays, and the high momentum antiprotons from $\overline{\Lambda}$ decays. For the upstream wall, only the E877 TOF detector was granular enough to give acceptable multiple hit probabilities.

---

[4]Looking down the beam, beam left refers to positions left of the beam. Beam right refers to positions right of the beam. Sometimes either are used to infer left or right of some reference point and not necessarily the actual beam.
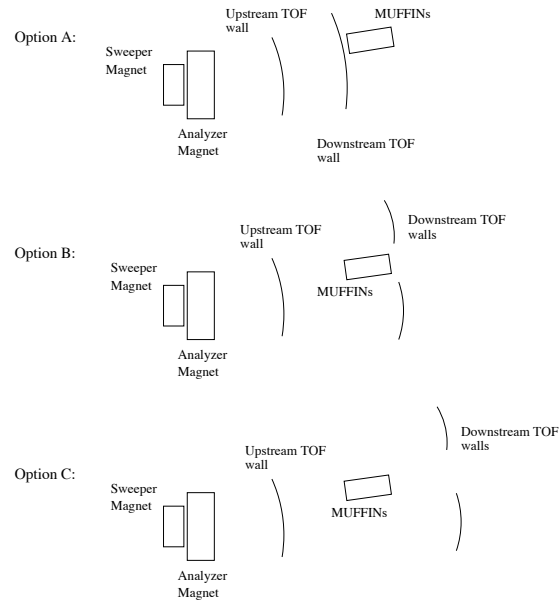
**Figure 2:** Options A, B, and C.

Option A was shown to be unacceptable because of a poor overall PID efficiency (flight path too short), and a poor geometric efficiency for measuring the low momentum pions in the upstream wall. In addition, the downstream wall in option A would have to be very granular (well exceeding the 45 slat constraint) because of the observed high multiple hit probabilities.

Options B and C were also shown to be unacceptable because of the very high number of hits on the downstream wall from secondaries produced in the MUFFINs. The simulations implied that a fourth configuration, called D, would outperform the A, B, and C configurations. Configuration D is shown in Figure 3. In this configuration, the detector used in E877 is flanked by two smaller side walls.

Option D:

Sweeper
Magnet

Analyzer
Magnet

MUFFINs
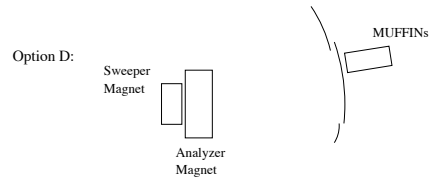
**Figure 3:** Option D.

For this configuration, the multiple hit probabilities in each slat is shown in Figure 4. HIJET events from central collisions (impact parameter b=0) were used, and all secondaries produced in interactions downstream of the target are included. The top plot in Figure 4 shows that the multiple hit probabilites in the highly granular central wall are less than 10%. The two side walls are positioned in relatively lower particle occupancy regions, and this allows for wider slats than in the central wall.

Figure 4 also gives the local x distributions on the TOF configuration D for the daughters of the four different parents that E896 is capable of measuring. One notices that the daughters of the Fid parents are closer to the center of the wall than that of the MC parents. The Fid events require that the parent particles decay in the DDC, and this hardens the momentum spectrum of the parents compared to the MC events. The higher momentum daughters from these parents are deflected less by the field of the analyzer magnet. These plots show that the TOF walls have a relatively high geometric efficiency for measuring all of the daughters for both Fid parents and MC parents.
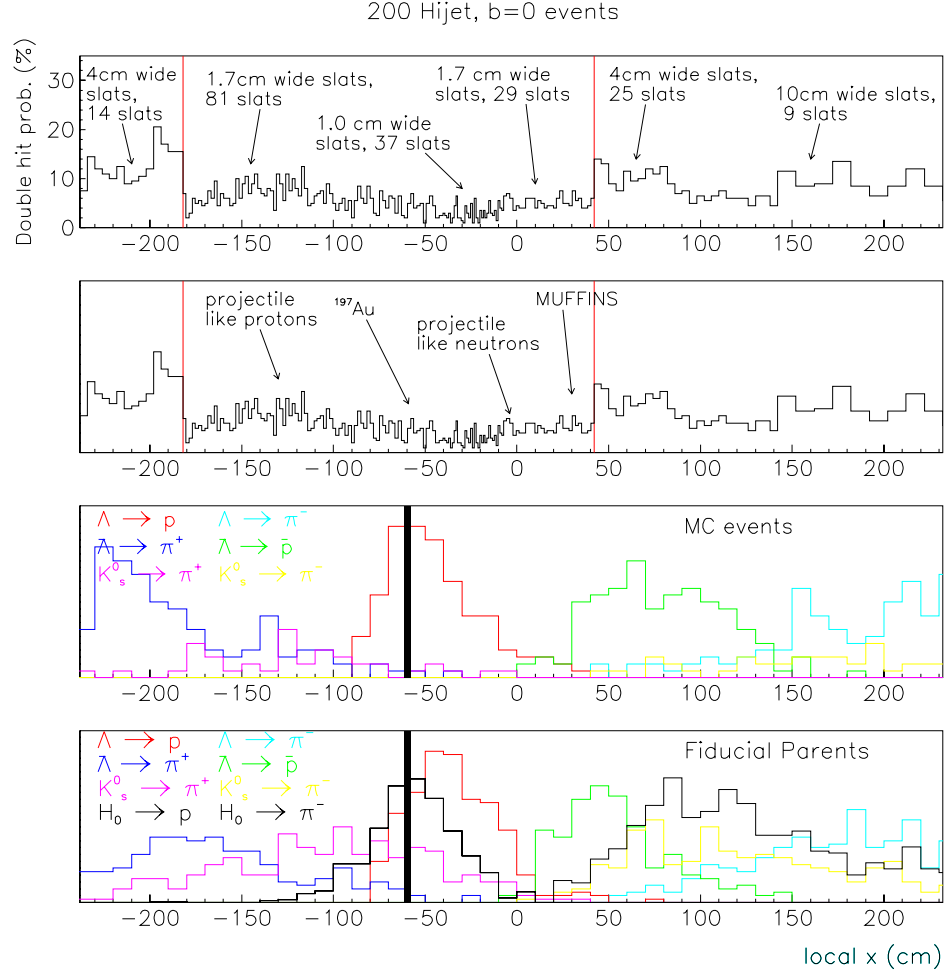
**Figure 4:** In the upper frames, the probabilities for two or more hits per slat versus the local x distribution. The bin widths in the upper two frames are the slat sizes used in the simulations. Below the top plot is a plot that shows where projectile like protons and neutrons hit the wall, where the gold beam would hit the wall, and the location of the MUFFINs detector behind the TOF wall. The term "projectile like" refers to particles that have rapidities close to that of the beam. In the lower two frames, the local x distributions as shown for the daughters of $H_0$, $\Lambda$, $\overline{\Lambda}$, and $K_s^0$ parents. Note the bin widths are not the slat widths in these lower two frames. The thick vertical lines in the lower frames indicates the local x position of the uninteracting Au beam.
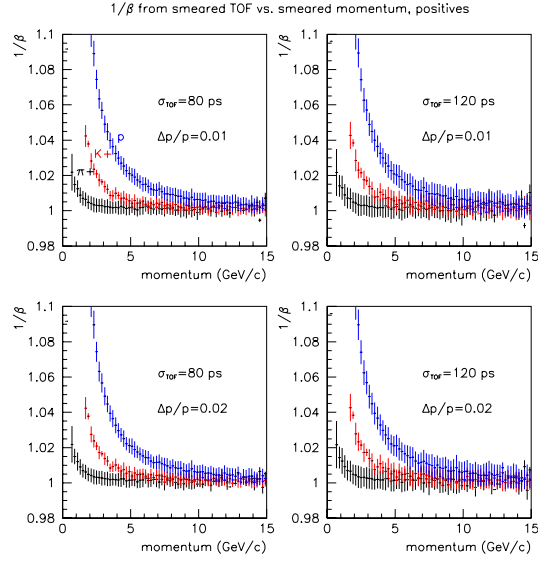
**Figure 5:** The $1/\beta$ versus momentum distributions for positively charged particle hits on the E896 TOF wall. The various frames show the results for different values of the momentum resolution and TOF resolution assumed in the simulations.

Figure 5 shows a plot of inverse velocity, $1/\beta$, versus the momentum for protons, positive kaons, and positive pions. The error bars shown in these plots correspond to the standard deviations. The cutoff momenta for $\pi^+/K^+$ separation and $K^+/p$ separation are determined from these plots for two different DDC momentum resolutions and two different TOF resolutions. Particles below the cutoff momenta can be identified directly with high efficiency and low background. The cutoff momenta are defined here to be the momentum at which the standard deviation bars for the TOF of the pions, kaons, and protons begin to touch. The cutoff momenta so defined are shown for positive and negative particles in Table 1. In general, the cutoff momenta

decrease as the momentum resolution decreases. Also, the cutoff momenta decreases as the TOF resolution decreases. These cutoff momenta are in the range 3 to 4 GeV/c for $\pi/K$ separation and 6 to 7 GeV/c for K/p separation.

The rates for measuring the different parent particles with the option D geometry is given in Tables 2 and 3. These rates are the numbers per event that pass the cut level listed. The $\overline{\Lambda}$ rates are calculated assuming the same multiplicity per event as the $\Lambda$. One should include factors on the order of a few times $10^{-3}$ for the actual production rate of $\overline{\Lambda}$ hyperons as compared to $\Lambda$ hyperons. The $H_0$ rates are calculated assuming 0.1 $H_0$ per central event. The rates per week are calculated assuming that 250 central events per second are written to tape, and that there are 100 hours of AGS beam per week.[5]

For the MC events shown in Table 2, the rates are 2 to 10 times higher than the rates for Fid events shown in Table 3. The rates are lower for the Fid events because of the requirement that the parent particle decay in the fiducial volume of the DDC. Many of the MC generated parent particles are reconstructable based on the TOF system even though they decayed upstream of the DDC.

Shortly before the 1997 gold run, radiation shielding blocks were inserted between the E896 beam area and an adjacent experiment. Because of this, the beam left wall in the D configuration was moved slightly forward and made narrower. The beam right wall was made slightly wider to use the extra available TOF slats. Shown in

---

[5]The design of the E896 data aquisition system and the trigger allows approximately 250 central events per second to be written to tape.

**Table 1:** The cutoff momenta for separating pions from kaons and kaons from protons. Below these momenta, particles are directly identifyable with high efficiency and low background. The uncertainty in these momenta is 0.3 GeV/c.

| Cutoff momenta | | | | |
|---|---|---|---|---|
| | $\Delta$p/p=1% $\sigma_{TOF}$=80ps | $\Delta$p/p=2% $\sigma_{TOF}$=80ps | $\Delta$p/p=1% $\sigma_{TOF}$=120ps | $\Delta$p/p=2% $\sigma_{TOF}$=120ps |
| $\pi^+/K^+$ | 3.7 GeV/c | 4.1 GeV/c | 3.2 GeV/c | 3.2 GeV/c |
| $\pi^-/K^-$ | 4.0 GeV/c | 3.8 GeV/c | 3.1 GeV/c | 3.0 GeV/c |
| $K^+/p$ | 6.9 GeV/c | 6.9 GeV/c | 5.8 GeV/c | 5.8 GeV/c |
| $K^-/\overline{p}$ | 6.8 GeV/c | 7.0 GeV/c | 5.6 GeV/c | 5.7 GeV/c |

**Table 2:** The rates per 100 hours of AGS beam for the MC events for the three different cuts, assuming 250 events per second written to tape.

| Rates from the MC events per week | | | | | | |
|---|---|---|---|---|---|---|
| | $\Lambda\to\pi^-$ | $\Lambda\to$p | $\overline{\Lambda}\to\overline{p}$ | $\overline{\Lambda}\to\pi^+$ | $K_s^0\to\pi^-$ | $K_s^0\to\pi^+$ |
| cut 2: | 1.52e7 | 3.90e7 | 8.47e7 | 9.72e6 | 1.08e7 | 3.99e6 |
| cut 3: | 9.36e6 | 9.36e6 | 8.60e6 | 8.60e6 | 1.07e6 | 1.07e6 |
| cut 4: | 9.54e5 | 9.54e5 | 9.99e5 | 9.99e5 | 1.53e5 | 1.53e5 |

**Table 3:** The rates per 100 hours of AGS beam for the Fid events for the three different cuts, assuming 250 events per second written to tape.

| Rates from the Fid events per week | | | | | | | | |
|---|---|---|---|---|---|---|---|---|
| | $\Lambda\to\pi^-$ | $\Lambda\to$p | $\overline{\Lambda}\to\overline{p}$ | $\overline{\Lambda}\to\pi^+$ | $K_s^0\to\pi^-$ | $K_s^0\to\pi^+$ | $H_0\to\pi^-$ | $H_0\to$p |
| cut 2: | 5.58e6 | 8.72e7 | 8.55e6 | 5.42e6 | 1.45e5 | 1.40e5 | 1.94e3 | 1.96e3 |
| cut 3: | 5.08e6 | 5.08e6 | 5.08e6 | 5.08e6 | 6.80e5 | 6.80e5 | 5.55e2 | 5.55e2 |
| cut 4: | 6.18e5 | 6.18e5 | 5.20e5 | 5.20e5 | 1.23e4 | 1.23e4 | 2.18e1 | 2.18e1 |
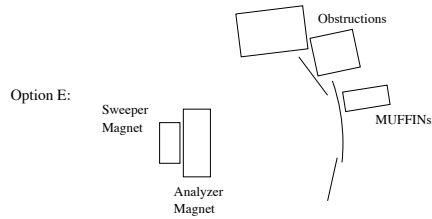
**Figure 6:** The final arrangement of the three TOF walls in E896.

Figure 6 is this configuration, called Option E. It is this E geometry that was proposed for the final configuration of the E896 TOF system. Given this design, the central wall was positioned and two smaller TOF detectors were constructed and positioned.

## IV. TOF Hardware and Electronics

The three TOF detectors consist of an existing TOF wall and two TOF walls built at Rice specifically for E896. The existing TOF detector was built by McGill University and used in BNL-AGS Experiment 877. The Rice University group assumed control of this detector in E896. It is positioned as the central TOF wall. The two side walls were built at Rice in late 1996 and subsequently positioned in the E896 beam area.

Even though the central TOF wall was already built, it took months of hard work to make it operational. Before positioning the wall in the E896 beam area, it required a complete uncabling and disassembly. Cables, patch panels, and discriminators were positioned to minimize scattering into the MUFFINs detector located directly behind the central TOF wall. Fifty bundles of twelve 600ns long RG-58 cables were routed from the counting house to the TOF detector. Connectors were replaced on almost

all these cables. Three hundred high voltage RG-59 cables were made and routed from high voltage power supplies outside of the experimental area to the central TOF array PhotoMultiplier Tubes (PMTs).

The central TOF array consists of 147 slats, all of which are 70cm long and 1.5 cm thick. Of the 147 slats, 118 are 1.7cm wide and 29 are 1.0 cm wide. An average time resolution of 81ps for all of the slats in the wall was observed in E877. [5] An average y-position (*i.e.* along the slat) resolution of 1.8cm was also observed in E877. [5]

There are are a total of 40 slats in the two side walls. All of the side wall slats are 5cm wide, 100cm long, and 1.5cm thick. Of these 40 slats, 26 slats are in the beam left wall and 14 slats are in the beam right wall. The slats are stacked side-by-side in aluminum unistrut frames. Bicron BC404 scintillator was used because of its fast 1.8ns decay time constant and acceptable 1.6m attenuation length.

A Hamamatsu 1398 PMT was directly glued to each end of the slat scintillator. This was done based on simulations comparing fishtail lightguides to direct contact of the PMT with the scintillator. [8] The slats were first wrapped with aluminum foil (except near the PMT photocathodes) and then wrapped with a layer of opaque plastic to optically isolate the slats.

In total, five LeCroy 1885F Fastbus charge-integrating analog-to-digital converters (ADCs) and seven LeCroy 1875A Fastbus time-to-digital converters (TDCs) were used to collect the TOF data. The ADCs digitize the analog pulse signals, and the TDCs digitize the time signals in 25ps bins. The TDCs are "common start" TDCs. They

measure the time between a start signal provided by the trigger and a stop signal provided by the TOF detector.
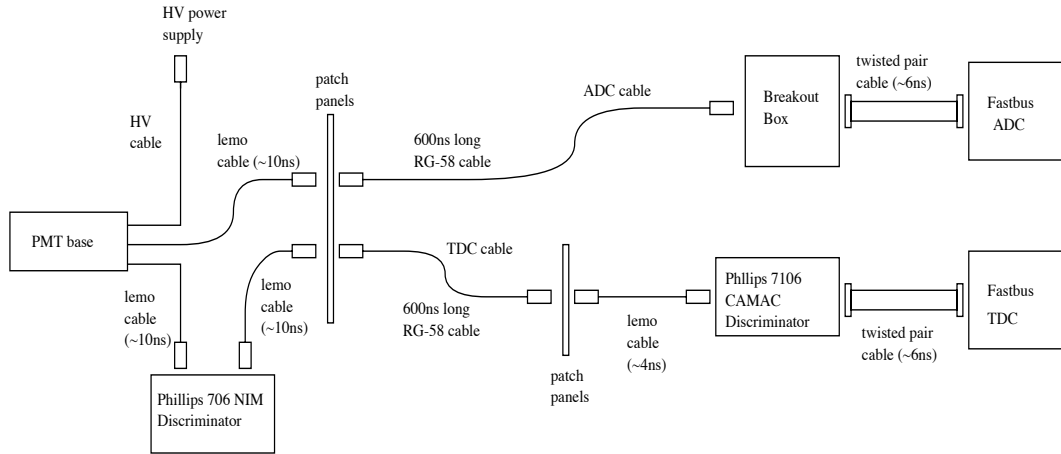


**Figure 7:**   There are two signal cables from each PMT. One cable is used for the pulse area measurement and the other is used for the time measurement. Both of these signals are cable delayed 600ns before being input to ADCs and TDCs. This long cable delay is required to allow for the trigger decision time.

As shown in Figure 7, the signals from each PMT are resistively split in each base into two equal amplitude outputs. One of the two signal cables is used for measuring pulse areas, while the other one is used for the time measurement. All TOF detector signals are sent through approximately 600ns of RG-58 cable to the TOF Fastbus crate in the counting house.

The TOF detector PMTs were powered by two daisy-chained LeCroy 1440 Power Supplies. A $^{90}$Sr beta source and a LeCroy 2467 image intensified oscilliscope were used at the TOF detector to set the voltage of each PMT. For a single PMT signal output cable, the PMT voltages were adjusted so that the PMT signals would have

a maximum pulse amplitude of 300mV at the detector, with the source held at the center of each slat. Some of the PMTs were weak and were set to less than 300mV. Instead of matching pulse areas (*i.e.* the ADC values), the pulse amplitudes were matched so as to give the best possible time measurement. This was done to equalize the rise time of the PMT pulses (with the source at the center of the slat), which is better determined by matching the pulse amplitudes. High voltage on the central wall PMTs varies from $-1300$V to $-2500$V, depending on the tubes and bases. High voltage on the side wall PMTs varies from $-1300$V to $-1900$V.

For the pulse area measurements, the raw PMT signals are sent through 600ns long 50$\Omega$ RG-58 cables to patch panels in the counting house, where they are then connected to Fastbus 1885F ADCs using approximately 6ns long 110$\Omega$ "twisted pair" cables. Instead of 110$\Omega$ twisted pair cables, 50$\Omega$ flat coaxial cables were originally tried to impedance match all the ADC cables. These coaxial cables were found to be more susceptible than the twisted pair cables to noise from the Fastbus power supply. With the Fastbus power supply on, a peak-to-trough ground noise of 33mV was measured for the coaxial cables. For the twisted pair cables, a 4.4mV peak-to-trough ground noise was measured. With the 110$\Omega$ twisted pair cables, the signal reflections from the impedance mismatch were acceptably small: less than one percent of the original ADC value after being reflected through 1200ns of RG-58 cable.

For the time measurement, one of the signal cables from each PMT is input to a Phillips 706 300MHz leading edge NIM discriminator placed next to the TOF detec-

tor. This was done to reduce the effects of dispersion, attenuation, and noise pickup that the raw signals would have experienced before being sent to the TOF Fastbus system through 600ns long RG-58 cables. Since the time measurement improves as the rise time of pulses decreases, it is best to discriminate the pulses where they have the fastest rise times — near the detector PMTs. The threshold of these discriminators was set to approximately 100mV. In the counting house, these signals were rediscriminated and converted to ECL by Phillips 7106 CAMAC discriminators before being input to the Fastbus LeCroy 1875A TDCs. These rediscriminated signals provide the stop signal for the TDCs.

The start signal from the beam counters was rediscriminated and fanned out three ways. One of these went directly to the LeCroy 1810 Calibration and Trigger (CAT) module to provide the TOF Fastbus busy signal for the E896 data acquisition system. The remaining two signals are used to provide the TDC start signals and the ADC gates. The TDC start signal was provided by cable delaying the fanned signal by approximately 110ns before signals arrived at the Fastbus TDCs. This cable delay was done to account for 50ns initial dead time within the TDC module, and an extra 60ns so the TDC signals would digitize in the linear mid-scale region of the TDC.

The ADC gate was set up by sending the third signal to a gate generator, and then through a cable delay. The ADC gate generally is set to start approximately 70ns before the raw analog signals arrive from the TOF detector PMTs. There is a 40ns initial deadtime in the ADC module, and one wants a few tens of ns room before

the earliest signals arrive. The ADC gate width was set to 200ns to accomodate the typical 130ns width of the analog signals (after passing through 600ns long RG-58 cables) and also leave a few tens of ns room afterwards.

It was discovered that all of the LeCroy Fastbus 1875A TDCs were much noisier than what would have been expected from the manufacturer specifications.[6] This noise is clearly seen in a simple test: a pulser is fanned into two signals, one is input into the TDC start and the other is cable delayed to be in the linear region of the TDC. Instead of a single TDC channel being recorded as expected, an RMS width of 3 to 5 channels is observed. The effects of this Fastbus noise will be discussed in the analysis in section VI, and comments on solving this problem are made in the final section.

## V.   Performance of the TOF detectors in the Experiment

The first data was taken during the last two weeks of January 1997 with an 11.7 GeV/c per nucleon $^{197}$Au beam on an $^{197}$Au target. The central TOF wall was up and in the data stream for this run.

The data obtained in this run was not ideal for the TOF analysis since the DDC performed very poorly.[7] To fully calibrate the TOF, one needs to use DDC tracking

---

[6]An RMS width of 1 channel is typical. An RMS width of 2 channels is the maximum.

[7]The DDC front end electronics were extremely noisy and produced false data in large regions of the DDC.

to account for differences in the TOF of particles with known momenta and path lengths.

Eight hours of data were taken in May 1997 with a secondary beam of protons and positive pions. All three TOF arrays were in the data stream during this run. The beam was swept across as much of the TOF walls as possible. This was done with the sweeper magnet turned off and varying an upstream beamline magnet (called D10) at four different analyzer magnet settings, ranging from zero field to full field.

There were three goals of this second run: to obtain relative TDC offsets of slats, to extrapolate "clean" tracks through the DDC (1 track in the DDC per event), and to develop software to extrapolate tracks through the analyzer magnet fringe fields to the TOF detector. The DDC was working properly during this beam run. Single tracks in the DDC are ideal for developing DDC tracking and calibration software. In addition, it is ideal for developing software to extrapolate tracks from the DDC to the TOF detectors. This data is useful for developing TOF calibration algorithms before the next six week gold beam run in spring of 1998.

In the remainder of this section, calibrations and analyses of the data from these two runs will be discussed. Specifically, pedestals and correlated noise will be investigated. Different methods for scaling the ADC gain data and two different slewing corrections will also be described. Throughout this data analysis, slats are referred to by unique "hole" numbers. These are positions in the TOF detector mounting structures where slats may be placed.
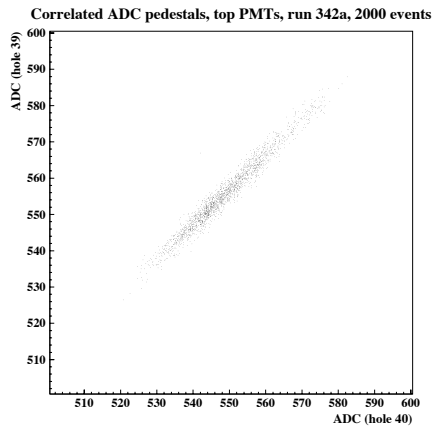
## A. Pedestals

When a PMT is not exposed to any light, a value is recorded by the ADC which is called the pedestal. There are two contributions to the pedestal: one is intrinsic to the ADC, and the other is the dark current of the PMT and any noise in the line.

Figure 8 shows two typical pedestal distributions for adjacent central TOF wall PMTs. In the left plot in Figure 8, the mean is at 555.8 channels, with an RMS width of 9.8 channels. The right plot in Figure 8 has a similar mean and RMS width. The mean of the distributions is drawn in the plots. The mean accurately estimates the center of the pedestal distributions for all the PMTs. These pedestal means are saved in TOF calibration files for subsequent analyses.
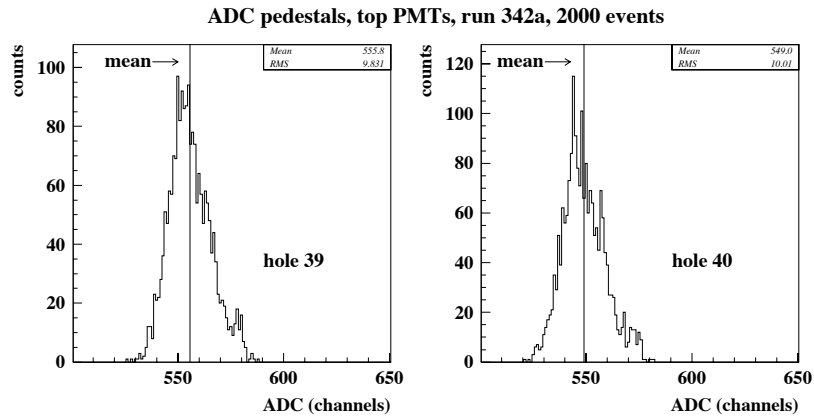


**Figure 8:** Two typical pedestal distributions. The mean is 555.8 channels in the left plot and 549.0 channels in the right plot. The RMS width of these distributions is ∼10 channels.

The pedestals in Figure 8 have a ~10 channel RMS width. These pedestals are very wide, and this is caused by significant amounts of correlated noise in the experiment. [10] Figure 9 shows the pedestal of one PMT versus the pedestal of another PMT. This plot shows that the pedestals are strongly correlated, which is verification of the presence of correlated noise in the experiment. Hardware plans to deal with this correlated noise are discussed in Section VI of this Thesis.



**Figure 9:**  This figure shows the pedestal of one PMT versus the pedestal of another PMT. This plot shows that the pedestals are clearly correlated, which is evidence for correlated electrical noise in the experiment.

## B.  ADC gains

Figure 10 shows two typical pedestal mean subtracted ADC distributions for a "hit" PMT. A PMT is considered to be hit if its TDC value is greater than zero. The clear peak in both of these ADC distributions corresponds to a single Minimum Ionizing Particle (MIP). The plot on the left in Figure 10 is from the gold run for a slat where

large numbers of primary protons are hitting. A small peak to the right of the MIP peak is seen. This corresponds to the pile-up of two MIPs in the same slat in one event. The plot on the right in Figure 10 is a pedestal subtracted ADC distribution from the secondary beam run. There is no pile-up peak seen, since each event has only one single charged particle.
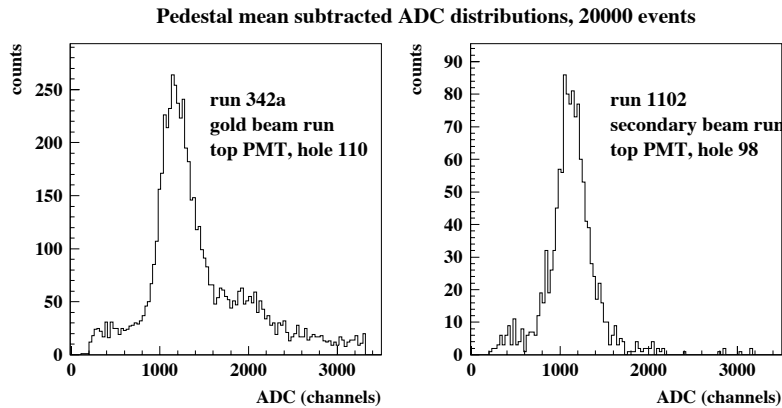


**Figure 10:** Pedestal subtracted ADC distributions. The plot on the left is from the gold run and the plot on the right is from the charge one secondary beam run. The peak in both plots corresponds to the MIP peak. In the left plot, there is a tail seen to the right of the MIP peak, which corresponds to the pile-up of two MIPS in a single event, three MIPS, etc. No pile-up peak is seen in the right plot, since there was only one particle per event in the secondary beam run.

Frequently, position-independent ADC and TDC values are useful. Both the top and bottom PMTs of a slat are used to calculate these quantities. A position-independent ADC value greatly reduces the effects of attenuation as light travels down the slat to the PMT. This attenuation is significant since the slats are about the same length as the attenuation length of the scintillator. Attenuation broadens

the ADC distribution of a single PMT. The position-independent ADC gives a value that depends primarily on the amount of light produced.

A position-independent TDC value is useful since it greatly reduces effects related to the travel time of light through the scintillator to the PMT. This effect broadens the TDC distribution of a single PMT. The position-independent TDC value gives a value that depends primarily on the TOF of the particle that hit the scintillator.

These position-independent ADC and TDC values will be labeled $\langle ADC \rangle$ and $\langle TDC \rangle$ throughout these analyses. They are defined as:

$$\langle ADC \rangle = \sqrt{ADC1 \cdot ADC2},$$

and

$$\langle TDC \rangle = (TDC1 + TDC2)/2,$$

where, for each slat, ADC1 and TDC1 refer to data from the top PMT, and ADC2 and TDC2 refer to data from the bottom PMT. A more thorough explanation of these definitions is given in Appendix A.

One is interested in pedestal subtracted $\langle ADC \rangle$ distributions that have been scaled so the MIP peak is at one. This is convenient since it allows one to define a scaled $\langle ADC \rangle$ range where single MIPs hit, where two MIPs hit, etc. The location of the MIP peak in an ADC distribution for a PMT is, in general, different for different PMTs. Even though two PMTs may produce pulses with the same peak amplitudes, the pulse shapes in general may be slightly different. These different pulse shapes thus have different areas and result in different ADC values. The MIP peak location also

depends on the ADC module and the pedestal. It is thus worthwhile to investigate methods to estimate the MIP peak from the ADC data from each PMT.

The following four methods to estimate this peak were investigated:

- mean: the mean of the ADC data is used to estimate the ADC location of the single MIP peak.

- maximum bin location: for a histogram of the ADC data, the location of the bin with the most counts is used to estimate the location of the single MIP peak.

- function fit: the ADC data histogram is fit with the function

$$f(ADC) = a \cdot exp((b - ADC)/2c - exp((b - ADC)/c)),$$

where a,b, and c are fit parameters determined by minimizing the $\chi^2$ of the fit. The location of the function's peak is at $b+c \cdot ln(2)$, the width of this function is related to the fit parameter $c$, and the fit parameter $a$ gives the normalization.

- limited range function fit: a histogram of the ADC data is fit with the same function, but over a limited range. The range is 0.85 to 1.35 of the location determined by the "maximum bin location" method.

Figure 11 shows a typical ADC distribution with estimates of the peak location for the four different methods. For this particular PMT, the high ADC value tail in the ADC distribution causes the "mean" method to overestimate the location of the peak. The "function fit" method underestimates the peak location since the fit is influenced by ADC data not just in the region of the peak. The "maximum bin location" method estimates the peak location accurately in this case, but this

**Pedestal mean subtracted ADC distribution, 20000 events**
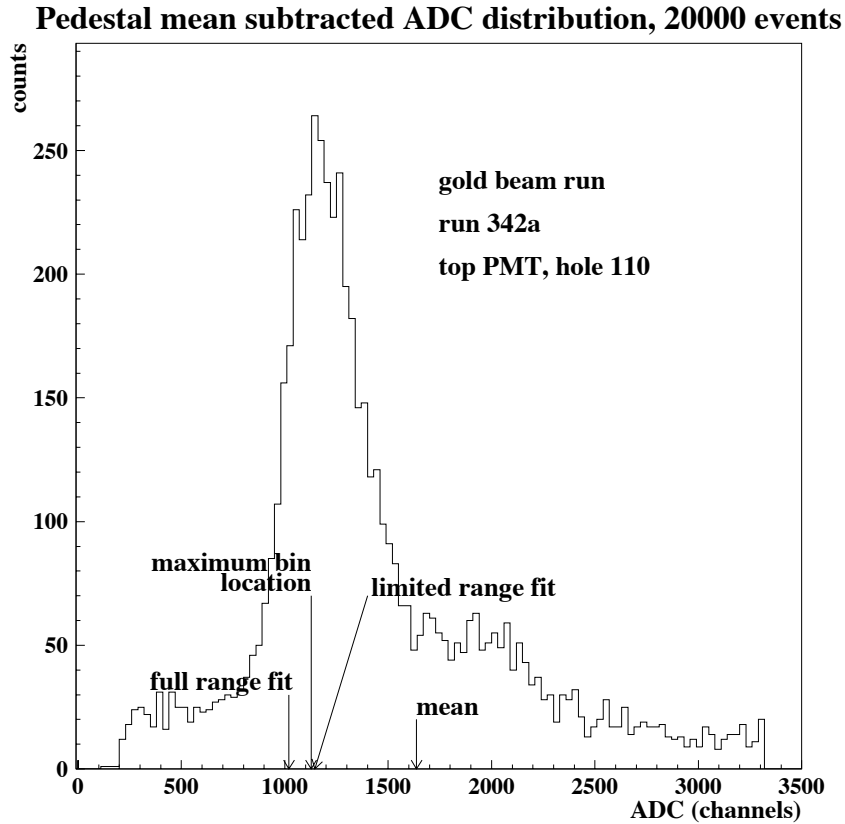


**Figure 11:** A typical pedestal subtracted ADC distribution for a slat in the Au run. Estimates of the MIP peak location using the four different methods are noted in the plot.

method is not ideal method for locating the MIP peak since it is sensitive to bin-to-bin statistical fluctuations. The "limited range fit" method accurately estimates the peak location, and unlike the "function fit" method, it has the advantage of fitting the ADC data only in the region of the MIP peak.

With only one ADC distribution investigated, conclusions cannot be drawn for analyzing the performance of the different MIP peak location methods. For some
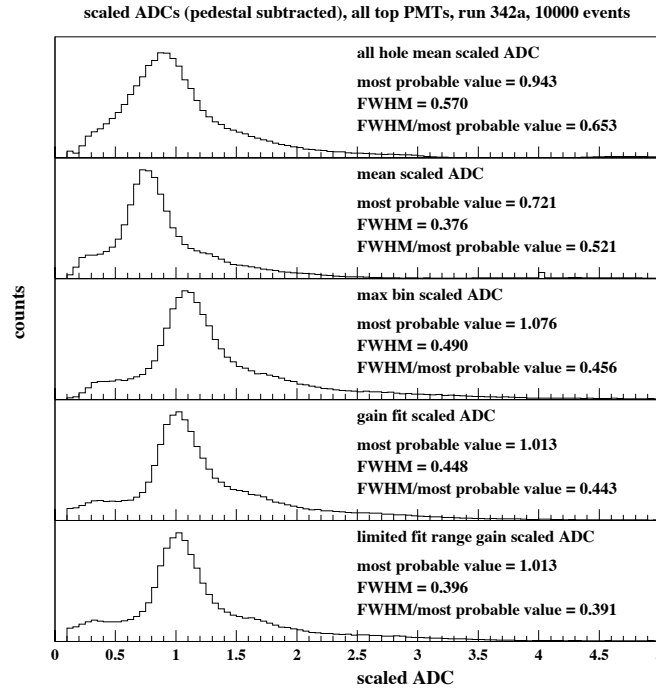
**Figure 12:** This shows scaled ADC distributions over all holes for different peak location methods. In the top figure, a single scale factor was used for all the PMTs. In the other plots, a scale factor determined for each PMT was used to scale the ADC values. The scale factor is supposed to set the MIP peak to unity. The methods improve going down from the top figure to the bottom figure. The best method has the smallest FWHM/most probable value, which is the "limited range fit" method.

of the individual distributions, some methods may work better than others. For example, the "mean" method and the "function fit" method may work well for an ADC distribution with very small tails. Therefore, it is worthwhile to investigate how the methods perform over all the TOF PMTs.

For a particular method, the gain scaled ADC distributions over all PMTs are widened for each incorrect estimate of the individual ADC distribution peaks. The

distribution of gain-scaled ADCs over all the top PMTs is shown in Figure 12 for the four different methods. The top plot in Figure 12 is an ADC distribution of all (top) PMTs using a single scaling value for all of the individual ADC distributions. The other four plots are ADC distributions of all the PMTs using scaling values appropriate for each PMT. This plot indicates which of the four methods is best for all of the PMTs, as the Full Width at Half Maximum (FWHM) divided by the Most Probable Value (MPV) is minimal for the best scaling method. For the five different methods, the worst method is seen in the top plot and the best method is seen in the bottom plot. The best method is the limited range gain fit, which has a FWHM/MPV=0.391. The next best method is the "function fit" method which has FWHM/MPV=0.443.

Shown in Figure 13 are ADC distributions of the top and bottom PMTs of typical slat fitted over the limited range as described above. The function fits the data very well and accurately estimates the MIP peak location.

The bottom plot in Figure 13 shows the gain-scaled $\langle ADC \rangle$ distribution, with the MIP peak scaled to one. One also sees a peak near 1.6 in Figure 13, which corresponds to a pile-up of two MIPs. This slat is in the region hit by large numbers of primary protons from central gold-gold collisions. This pile-up peak is not at 2.0 because the PMT response is nonlinear, which comes from running the bases above their recommended maximum voltage to achieve the fastest possible rise times. The location of the pile-up peak is consistent with that seen in E877. [5] For this slat,
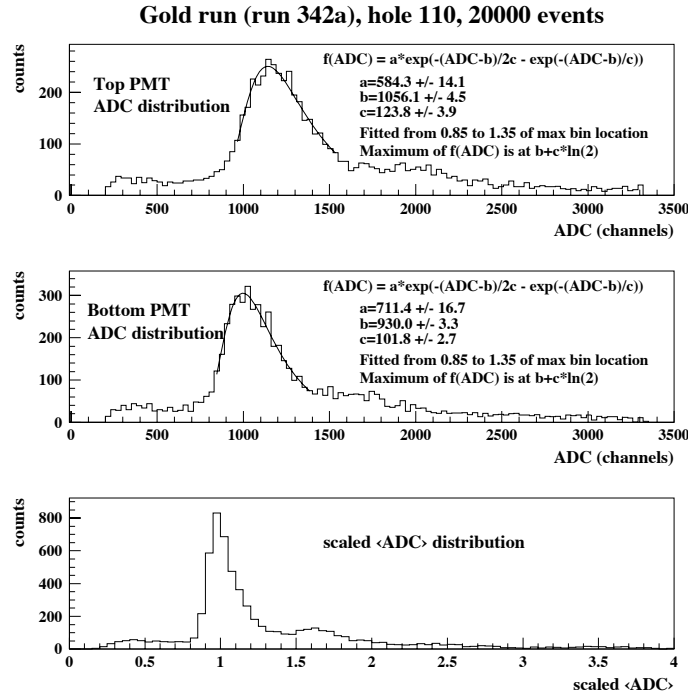
**Figure 13:** The ADC distributions for one slat in the gold run. The top two plots are the pedestal subtracted ADC distributions for the top and bottom PMTs. Each of these distributions is fit using the limited range fit method. The fit for both of these distributions is drawn in the plots. The bottom plot is the $\langle ADC \rangle$ distribution after using the scale factors obtained from the top two plots. The MIP peak is scaled to unity and the fractional resolution is $\sim$20%.

a fractional resolution of $\sim$20% is observed in the bottom plot in Figure 13. This is consistent with the average $\sim$16% value observed over the entire McGill TOF detector in E877. [5]

The MIP locations determined by all four different methods are stored in the TOF calibration file for public use. Even though the calibration data from the limited range

fit method is the only one used for scaling the ADC values, the results from the other methods are useful for recognizing problems with the system.
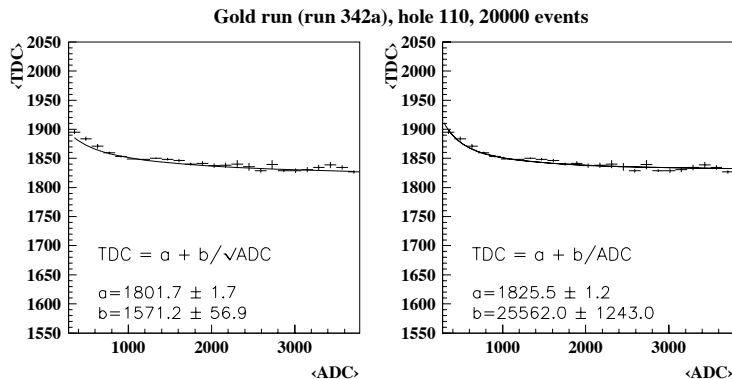
## C.   Slewing Corrections

The term *slewing* refers to the time-walk associated with particles that simulataneously hit a slat and which produce different amplitude pulses within the PMTs. The rise time of pulses generally depends on the pulse amplitude. Specifically, the rise time decreases as the pulse amplitude increases. Since the measured time is determined by when a pulse crosses a fixed discriminator threshold, particles that hit a slat at the same time but produce different amplitude pulses will result in different measured TDC values. The TDC value for a large pulse will be less than the TDC value time for a smaller pulse even if their arrival times are exactly the same.
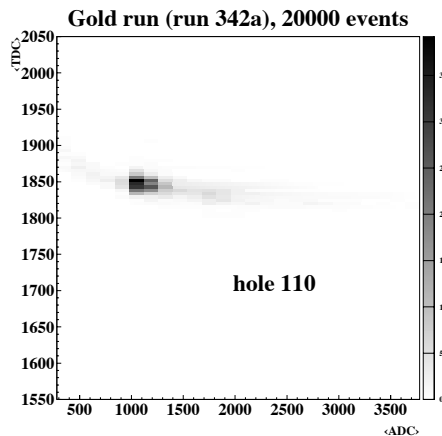


**Figure 14:**   A typical $\langle TDC \rangle$ *vs.* pedestal subtracted $\langle ADC \rangle$ distribution for a slat. The slewing effect is clearly seen; as the $\langle ADC \rangle$ value increases, the $\langle TDC \rangle$ value decreases.

Rather than measure the pulse amplitudes, the ADCs are used in the following slewing descriptions since they already roughly estimate the pulse amplitudes. The slewing effect is clearly seen in Figure 14. Larger $\langle ADC \rangle$ values result in smaller measured $\langle TDC \rangle$ values. The slewing effect can be corrected as now described.

This correction is done on unscaled pedestal subtracted $\langle ADC \rangle$ data and raw $\langle TDC \rangle$ data. Commonly, the slewing is assumed to be either a $1/\langle ADC \rangle$ or $1/\sqrt{\langle ADC \rangle}$ dependence, [11] where the $\langle ADC \rangle$ is the pedestal subtracted value. The functions $\langle TDC \rangle = t_0 + c/\sqrt{\langle ADC \rangle}$ and $\langle TDC \rangle = t_0 + c/\langle ADC \rangle$ are fit to the $\langle TDC \rangle$ *vs.* $\langle ADC \rangle$ data for each slat, with $t_0$ and c as fit constants to be determined for each slat. The two plots in Figure 15 show these fits for one slat in the gold run for the two slewing forms. In the $1/\sqrt{\langle ADC \rangle}$ fit shown in the left plot of Figure 15, the number of Degrees Of Freedom (DOF) is 23 and $\chi^2/\text{DOF}=13.4$. A $\chi^2/\text{DOF}=2.6$ with DOF=23 is obtained from the $1/\langle ADC \rangle$ fit shown in the right plot of Figure 15.



**Figure 15:** The fit of the average $\langle TDC \rangle$ versus the $\langle ADC \rangle$ for the two functional forms for the slewing. The error bars are the errors in the mean.

Depending on which slewing form is used, the slew corrected $\langle TDC \rangle$ is either $\langle TDC \rangle = \langle TDC \rangle_{measured}$ - $c/\langle ADC \rangle$ or $\langle TDC \rangle = \langle TDC \rangle_{measured}$ - $c/\sqrt{\langle ADC \rangle}$. Figure 16 shows the $\langle TDC \rangle$ distributions for a slat from the gold run before and after the slew corrections for both slewing forms. The results show minimal differences between the two different slewing corrections. The $\langle TDC \rangle$ distributions become $\sim 30\%$ narrower after the slew corrections. With the ADC time dependence removed, the width of the distribution now depends on the time spread of particles that hit the slats (which depends on the variations in path length and momenta), the Fastbus TDC noise (described in section IV), and the time resolution of the TOF detector and beam counters (which provide the start time for each event).
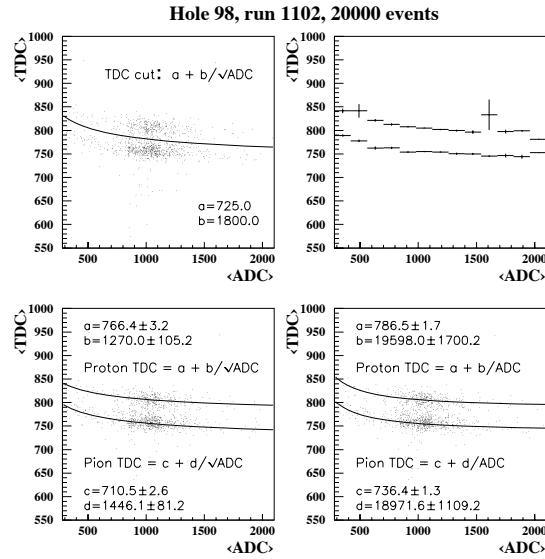
Shown in Figure 17 are the $\langle TDC \rangle$ vs. $\langle ADC \rangle$ distributions from the secondary beam run. Two separate $\langle TDC \rangle$ vs. $\langle ADC \rangle$ distributions are observed for the protons and pions, with the pions having the lower $\langle TDC \rangle$ values. A cut to separate these two distributions is shown in the top left plot of Figure 17. The $\langle TDC \rangle$ vs. $\langle ADC \rangle$ data of the pions and protons are then separately fit with the two different slew functions. The two plots in Figure 17 show these fits for one slat for the two slewing forms. In the bottom left plot, the fit for the pions has a $\chi^2/\text{DOF}=1.0$ and the fit for the protons has a $\chi^2/\text{DOF}=1.3$. In the bottom right plot, the slew fits result in a $\chi^2/\text{DOF}=1.0$ for the pions and $\chi^2/\text{DOF}=0.7$ for the protons. In all of these four fits, DOF=14.
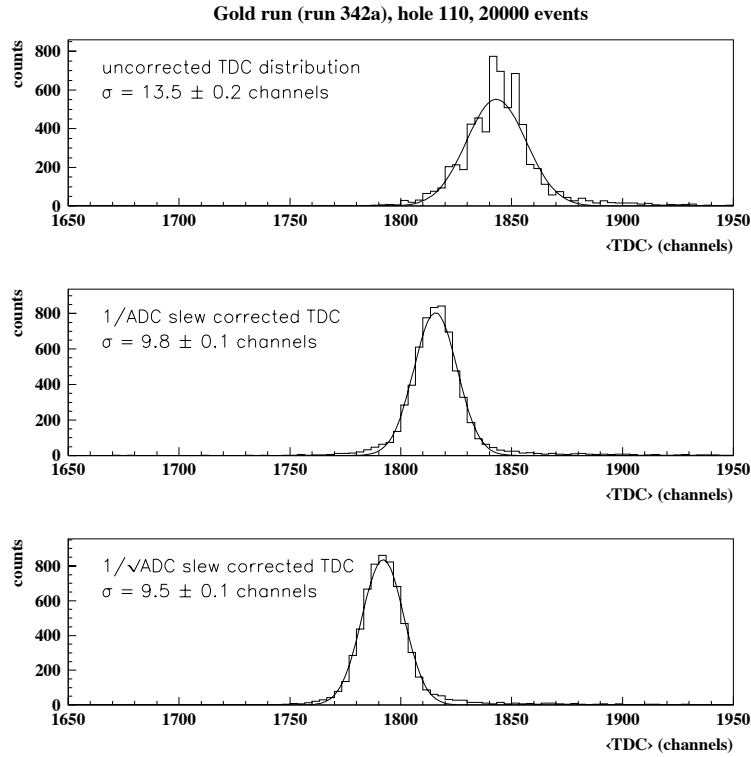
**Figure 16:** $\langle TDC\rangle$ distributions from one slat in the gold run. The top plot is a raw $\langle TDC\rangle$ distribution, and the two bottom plots show the same $\langle TDC\rangle$ distribution after slew corrections using the two different functional forms. Before slew correcting, the $\langle TDC\rangle$ width in the top plot is 13.5 channels. The width of each slew corrected $\langle TDC\rangle$ distribution is ∼30% narrower, or on the order of 9.7 channels.

Using data from the secondary beam run, Figure 18 shows $\langle TDC\rangle$ distributions for a single slat before and after slew corrections. In each of the three plots, two separate $\langle TDC\rangle$ peaks corresponding to protons and positive pions are observed. In the bottom two plots, the slew corrected $\langle TDC\rangle$ values are shown for the two slew correction

**Figure 17:** $\langle TDC \rangle$ *vs.* $\langle ADC \rangle$ distributions for one slat from the secondary beam run. Two separate distributions corresponding to protons and positive pions are observed. A cut to separate these particles is shown in the top left figure. The top right figure shows the $\langle TDC \rangle$ *vs.* $\langle ADC \rangle$ in a profile histogram for the protons and pions separately using this cut. Fits of these separate distributions are shown in the bottom two plots for the two different slewing functional forms.

forms. The two corrections result in similar distribution widths, approximately 10% to 15% narrower for this slat.

For this run, if one assumes there are minimal variations of the path length of particles that hit a single slat, the width of the $\langle TDC \rangle$ distribution can then attributed to the time spread of particles (from the momentum spread only) hitting a slat, the Fastbus TDC noise, and the time resolution of the beam counters and TOF slat. Accounting for the time effects of the momentum spread and noisy Fastbus TDCs,
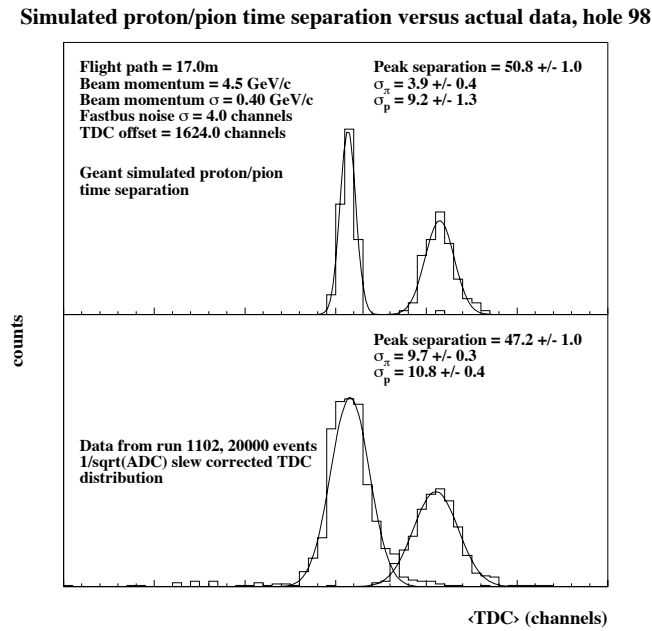
**Hole 98, run 1102, 20000 events**
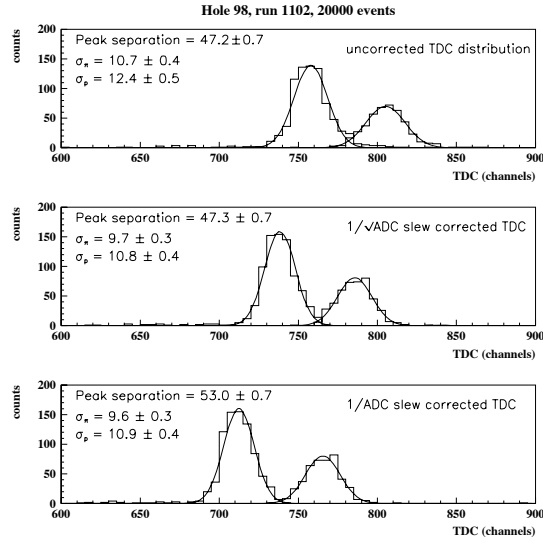
**Figure 18:** $\langle TDC \rangle$ distributions from the secondary beam run before and after separate slew corrections for the protons and positive pions. The two bottom plots show slew corrected $\langle TDC \rangle$ for two different slewing functional forms. The slew corrections make the $\langle TDC \rangle$ distributions 10% to 15% narrower.

an intrinsic time resolution for the system can be estimated from simulations, as now described.

Using the $\langle TDC \rangle$ distributions for the protons and pions, an estimate of the time resolution of TOF hole 98 can be made. With a ∼17.0m estimate of the path length of the beam from the beam counters to TOF hole 98, a ∼4.5 GeV/c momentum is estimated using the ∼50 channel TDC peak separation (∼1.125ns) of the protons and pions shown in Figure 18. Preliminary results from DDC tracking software indicate the beam momentum spread is ∼10% of the mean momentum. Using a 4.5±0.4 GeV/c beam momentum, a GEANT simulation was done to track pions and protons

over this flight path from the beam counters to hole 98. Included in this simulation
was the typical measured 4.0 channel (25ps/channel) RMS noise from the Fastbus
TDCs (which was measured as 4±1 channels) described in Section IV.



**Simulated proton/pion time separation versus actual data, hole 98**

Flight path = 17.0m
Beam momentum = 4.5 GeV/c
Beam momentum $\sigma$ = 0.40 GeV/c
Fastbus noise $\sigma$ = 4.0 channels
TDC offset = 1624.0 channels

Geant simulated proton/pion
time separation

Peak separation = 50.8 +/- 1.0
$\sigma_\pi$ = 3.9 +/- 0.4
$\sigma_p$ = 9.2 +/- 1.3

Peak separation = 47.2 +/- 1.0
$\sigma_\pi$ = 9.7 +/- 0.3
$\sigma_p$ = 10.8 +/- 0.4

Data from run 1102, 20000 events
1/sqrt(ADC) slew corrected TDC
distribution

‹TDC› (channels)

counts

**Figure 19:** TDC distributions. The top plot shows simulated TDC data and
the bottom plot shows slew corrected TDC distributions from the secondary
beam run. For the pion TDC distribution, the width of the simulated data is
3.9±0.4 channels while that of the actual data is 9.7±0.3 channels. For the
protons, the width of the simulated data is 9.2±1.3 channels and the width of
the slew corrected time distribution is 10.8±0.4 channels.

Figure 19 shows a slew corrected TDC distribution for hole 98. The upper plot
shows the results of the simulated data and the lower plot shows the actual slew cor-
rected data. The simulated TDC data includes the effects of momentum spread and
TDC noise. The difference in the simulated distribution and the actual distribution is

attributed to the time resolution of the beam counters and the TOF slat. This difference can be calculated in quadrature since the errors are independent. Thus for the pions, the time resolution is $\sigma=\sqrt{9.7^2 - 3.9^2} = 8.9$ channels, which is approximately 222.5 ps. For the protons, the time resolution is $\sigma=\sqrt{10.8^2 - 9.2^2} = 5.7$ channels, or 142.5 ps. Since the time resolution of the protons and pions differ so greatly, there is a discrepancy which will be investigated as now described.

To understand the interplay of path length variations and momentum variations on the observed TOF widths, an intrinsic time resolution of 100ps for the TOF slat and the beam counters is assumed. Removing this 100ps (4 channel) contribution in quadrature from the observed slew corrected TDC distributions, 7.9±1.1 channels and 9.2±1.1 channels are obtained for the pions and protons, respectively. The variation in momenta and path lengths consistent with these values will now be determined.

Using a Monte Carlo approach, the momenta and path lengths of pions and protons were independently varied and time distributions were obtained using the equation $TOF = (d/c)\cdot \sqrt{1 + m^2/p^2}$. For the pions, using an unrealistically large momentum variation of 4.0 GeV/c and 0.0cm path length variation, the width of the time distribution is very small ($\sigma=1.1$ channels) compared to 7.9 ±1.1 channels calculated above. This implies that the momentum variation alone contributes only a small amount to the time spread observed for the pions. Using a 0.45 GeV/c momentum spread and a 2cm path length variation, a time spread of $\sigma=2.3\pm0.1$ channels is observed. Using the 0.45 GeV/c momentum spread but a 6cm path length variation,

$\sigma$=7.9±1.1 is observed. Using a slightly larger length variation of 7.0cm, a $\sigma$=9.3±0.3 is observed with a 0.45 GeV/c momentum spread. Given the insensitivity of the time distribution to the momentum spread of the pions, it is unknown how large the momentum spread actually is. Nevertheless, using the 6cm path length variation and the estimated 0.45 GeV/c momentum variance produces a time variation consistent with the 7.9±1.1 channel value calculated above.

For the protons, first ignoring path length variations, and using the expected 0.45 GeV/c momentum variance, a 9.3±0.4 channel variation is obtained. At 1.0cm path length variance and 0.45 GeV/c momentum variance, a 9.8±0.3 channel variation is obtained. To investigate the sensitivity of the proton time distribution on momentum variance, a 0.9 GeV/c is assumed with 0.0 cm length variance. This results in a 14.5±0.6 channel variation, which is too wide for the 9.2±1.1 value calculated above. These studies show the proton time distribution is very sensitive to both the variance in the momentum and the variance in the path length.[8] A 0cm to 1cm path length variance and 0.45 GeV/c momentum variance gives a time distribution consistent with the 9.2±1.1 channel calculated value.

Summarizing these results, the time spread of the pions cannot be explained from momentum variance alone. The width of the pion TDC distribution is primarily determined by path length variance. By comparing the time spread of the actual TDC distribution (with the contributions from the Fastbus noise and intrinsic time

---

[8]Protons are more sensitive to momentum spread than pions because of their higher mass. The mass determines how important the term $m^2/p^2$ is in the equation $TOF = (d/c) \cdot \sqrt{1 + m^2/p^2}$.

resolution of the TOF detector and beam counters removed in quadrature) to Monte Carlo generated distributions, A 6cm path length variance was determined for the pions using the estimated 0.45 GeV/c momentum variance. Unlike the pions, the time spread of the protons is sensitive to both momentum variance and path length variance. Using the estimated 0.45 GeV/c momentum variance for the protons, a path length variance of less than 1cm was determined. The discrepancy described above can be explained by a difference in path length variance between pions and protons in the secondary beam.

The possible differences in momenta variance and path length variance between pions and protons are interesting questions that will be answered in the next data set. That data set will be free of the correlated noise and Fastbus TDC noise, just to name some improvements that will be made for the next run, as discussed in the final section of this Thesis.

## VI.   Conclusions and Outlook

E896 is an experiment designed to search for weak decays of the $H_0$ dibaryon. The design of E896 also allows for the studies of other strange neutral particles that decay weakly, such as $\Lambda$ and $\overline{\Lambda}$ hyperons and $K_s^0$ mesons. There are many significant backgrounds for reconstructing these particles based on tracking alone. A TOF detector greatly decreases these backgrounds by providing direct PID of these decay daughters. This motivated the design of a TOF detector using simulations.

The optimal TOF detector geometry was found among several options and some number of contraints that would be sensitive to the daughters of the $H_0$, $\Lambda$, $\overline{\Lambda}$, and $K_s^0$. Rates were given for identifying these daughters for three cuts using simulated data from the TOF detector.

Based on these simulations, a large, highly granular existing detector was positioned as the central TOF detector. Extensive work disassembing this central wall was done before before positioning it. In its final position, that wall was rebuilt so to minimize scattering of particles into the MUFFINs detector located downstream of the TOF detectors. Two side wall TOF detectors were built at Rice. These aluminum unistrut supported detectors were subsequently positioned according to the optimal simulated TOF detector geometry. The central wall was in the data stream for the 1997 gold beam run and all three TOF walls were in the data stream for the 1997 charge one secondary beam run.

The data shows there is significant correlated noise throughout the experiment. Plans to minimize this problem are discussed in the next section.

Methods to estimate the location of the MIP peak were discussed. These methods were first investigated for an individual PMT. They were then investigated over all the TOF detector PMTs. The "limited range fit" method was found to be the best method.

Two different methods to slew correct the TDC data were discussed. Two slewing functional forms were fit to the TDC *vs.* ADC data to obtain slew correction

parameters. Using these parameters, the slew corrected TDC distributions for both methods were given. Both methods result in similar slew corrected TDC distribution widths.

Pions and protons are observed in the data from the secondary beam run. For a single slat, separate slew fits of the pions and protons were done on the TDC *vs.* ADC data. The TDC data was for pions and protons were then individually slew corrected.

A GEANT simulation was done to determine the width of the TDC distributions from the momentum spread of the beam and noise from the Fastbus TDCs. Comparing the simulated TDC data to the observed TDC data, a time resolution was given for one of the the slats with the beam counter resolution included. Since the time resolution of protons and pions were very different, the effects of path length variation were instigated with a monte carlo approach. It showed that the width of the pion distribution was primarily determined by path length variations. The width of the proton distribution was primarily determined by both momentum variations and path length variations.

## A.   Joblist

Plans to improve the TOF detectors for the spring 1998 gold beam run are now discussed. The Rice walls will be refurbished before the 1998 gold run. Specifically, the PMT and base junctions will be improved, the PMTs will be reglued to the slats, and the slats will be rewrapped with Tyvek instead of aluminum. Tyvek is more

reflective than aluminum and is expected to increase the light output of each slat by ∼30%. [9]

It is suspected that the noise in the TDCs is related to the way the TOF DAQ is setup. The DAQ software will be rewritten and tested before the 1998 gold run.

In the 1997 gold run and 1997 secondary beam run, the beam counter signals were recorded in the MUFFINs Fastbus DAQ system. During the 1998 gold run, the beam counter signals will be input to each TOF Fastbus TDC to reduce noise variations among different Fastbus modules.

The time calibration of the Fastbus LeCroy 1875A TDCs will be done several times during the 1998 gold run using an Ortec 472 time calibrator. A time calibration is required since one TDC channel, in general, does not equal 25ps/count, as quoted by the manufacturer. The time per channel depends on temperature, the TDC module used, etc. It is thus worthwhile to time calibrate all the TDCs many times during the upcoming beam run to account for these variations.

Problems were seen in current cable map. The cable map determines which PMT is connected to which ADC channel and TDC channel. There are a few mismatched cables that will be corrected. This will done using a radioactive source at the TOF detectors and online data monitoring programs. The source will be placed next to a single slat to make its PMTs "fire". Relating the hit PMTs to their ADC and TDC channels can be done easily with this method.

A 60Hz scalar will be used to monitor the phase of the AC line to subtract the correlated noise. It is currently being built at Rice University. Sources of correlated of noise will also be thoroughly investigated. All electronics in the experiment will be turned on one at a time while monitoring the ground with an oscilloscope.

Time offsets will be monitored closely throughout the duration of the 1998 gold beam run. Offsets can change from radiation damage in the slat scintillators or temperature changes. These offsets will be obtained by comparing the calculated TOF to the measured TOF for known particles. To do this, software that extrapolates tracks from the target to the TOF wall is used.

## Appendix A. Position-independent ADCs and TDCs

There are three things important to understanding position-independence:

1) the amount of light produced by a particle that travels through the scintillator.

2) the light is attentuated exponentially as it travels down the slat to the PMT. This was observed for the central wall slats in E877. [5]

3) the measured TOF includes the time of travel of light through the scintillator to the PMT.

The following position-independent values are used:

$$\langle ADC \rangle = \sqrt{ADC1 \cdot ADC2},$$

and

$$\langle TDC \rangle = (TDC1 + TDC2)/2,$$

where ADC1 and TDC1 refer to the top PMT, and ADC2 and TDC2 refer to the bottom PMT for each slat. If L1 is the distance from the slat hit to the top PMT, and L2 is the distance from the slat hit to the bottom PMT, then L1+L2 is the length L of the slat. For a scintillator with attenuation length $a$, the geometric mean of the top and bottom ADC values is given by:

$$ADC1 = C1 \cdot exp(-L1/a) \text{ and } ADC2 = C2 \cdot exp(-L2/a)$$

$$\langle ADC \rangle = \sqrt{ADC1 \cdot ADC2} = \sqrt{C1 \cdot C2 \cdot exp(-(L1+L2)/a)}$$

$$\langle ADC \rangle = \sqrt{C1 \cdot C2 \cdot exp(-L/a)}$$

This ADC definition is independent of the hit position and only depends on the amount of light produced.

The speed of light travels down the slat according to the index of refraction and according to the geometry of the slat. An effective velocity $\langle v \rangle$ (which has to be measured) has to be used in calculations since the light bounces off the slat walls as it travels to a PMT. E877 measured an average $\langle v \rangle$ of 15.4 cm/ns. [5]

$$TDC1 = TOF + L1/\langle v \rangle \text{ and } TDC2 = TOF + L2/\langle v \rangle$$

$$\langle TDC \rangle = (TDC1 + TDC2)/2 = TOF + (L1+L2)/2\langle v \rangle$$

$$\langle TDC \rangle = TOF + L/2\langle v \rangle$$

Now $L/2\langle v \rangle$ is just a constant which contributes to the time offset. Therefore, the arithmetic average of the top and bottom TDC values of a slat is independent of the hit position on the slat.

# Bibliography

[1] Jaffe, R. L., "Perhaps a Stable Dihyperon," *Phys. Rev. Lett.*, **38**, 195-198 (1977).

[2] Llope, W. J., "The BNL-AGS Experiment 896," *Adv. Nucl. Dynamics 2*, 19-28 (1996).

[3] Crawford, H. J., Hallman, T.J., *et al.*, "A Proposal to the BNL-AGS: To Search for a Short-Lived H Di-Baryon, Short Lived Strange Matter, and To Investigate Hyperon Production in 11.6A·GeV/c AuAu Collisions," AGS Proposal 896.

[4] Rotondo, F., "Backgrounds induced by photon and strange hadron reactions in the DDC," E896 Note, March 1995; E. Judd, "Neutron-induced backgrounds in the DDC," E896 Note, March 1995.

[5] Lacasse, R., Ph.D. Thesis, McGill University, unpublished.

[6] Greiner, L., private communication.

[7] Shor, A. and R. Longacre, "Effects of secondary interactions in proton-nucleus and nucleus-nucleus collisions using the HIJET event generator," *Phys. Lett. B*, **218**, 100-104 (1989).

[8] Mutchler, G., private communication.

[9] Llope, W.J., private communication.

[10] Kainz, K.K., "Design, Construction, and Commissioning of the Exit Charge Detector for BNL-AGS Experiment 896," Masters Thesis, Rice University, unpublished.

[11] Sugitate, T., *et al.*, "100cm Long Time-of-Flight Scintillation Counters with RMS Resolution of 50 ps," *Nucl. Inst. Meth.*, **A249**, 354-360 (1986).